Electronic Supplement to: Narrowband Signals Recorded Near a Moulin that are Not Seismic Moulin Tremor: A Cautionary Short Note

Joshua D CARMICHAEL[1*]

[1]*Los Alamos National Laboratory, Los Alamos NM, USA*

Correspondence: Joshua D Carmichael <joshuadc@lanl.gov>

SUMMARY

Our electronic supplement supports installation concepts, waveform features, and signal detection methods summarized in the main article. Installation Methods condenses some unpublished geophone and seismometer deployment schemes that cryoseismologists have used in the field. These methods were shared with the author over email, in response to a Cryolist inquiry (Table S1). Geophone NLBS Data Spectrograms documents North (ELN) and vertical channel (ELZ) spectrogram figures (Figure S1) that we computed from the NLBS geophone over the same time duration (DOY 170-250, 2011) as shown for channel NBLS.ELE in Figure 2 of the main article. Low Frequency Seismic Events includes a figure (Figure S2) that shows longer duration seismic waveforms that record earthquake or icequake events below the 4.5 Hz natural frequency of the L-28 geophones that were deployed at the North Lake site. Finally, Correlation Detectors develops both theoretical and practical aspects of processing geophone data that records glaciogenic and resonance signals with a multichannel correlation detector.

* Present address: MS D446, P.O. Box 1663, Los Alamos NM, 87545

INSTALLATION METHODS

This section condenses some unpublished geophone and seismometer deployment schemes that cryoseismologists have used in the field. These methods were shared with the author over email, in response to a Cryolist inquiry (Table S1).

Table S1. A list of respondent messages to an October 26, 2018 CryoList email (http://cryolist.org/) request for installation titled "deployment tricks for preventing geophone melt-out: references?" sent by the author to list serve cryolist@lists.cryolist.org.

Investigators/Respondents: Nathan Stevens and Luke Zoet.

Installation Method: Mount geophones on a "wave-guide" that consists of a well-engineered pole and install the geophone-pole system into the ice surface, to delay melt out.

Recovery Details: None reported.

Sensors: Inexpensive geophones.

Deployment Site: Ablation zones like the Greenland Ice Sheet.

Investigators/Respondents: Ginny Catania and Jose Rial.

Installation Method: Drill holes in ice with large diameter auger to seat sensors well below ice and delay eventual melt out (images above).

Recovery Details: High quality retrieved data.

Sensors: L-22 or L-28 geophones and broadband sensors.

Deployment Site: Western Greenland Ice Sheet.

Investigators/Respondents: Marianne Karplus and Galen Kaip.

Installation Method: Deploy nodes that include sensor, data logger, and battery, under ≥ 1m of snow; attach nodes to aluminum seating plates (images above).

Recovery Details: deployment period included mid-June to mid-July 2017. Sensors melted out in 10 days. Snow under plates differentially melted out, which caused the plates and nodes to tilt, sometimes significantly. Some sensors likely rotated during melt out. Imprint of melt out in time series not reported.

Sensors: Fairfield Nodal Z-Land 3-C 5-Hz nodes (all-in-one geophone and datalogger and battery).

Deployment Site: Lemon Creek Glacier (Juneau Icefield, AK).

Investigators/Respondents: Tim Bartholomaus.

Installation Method: Drill narrow-diameter holes with several flights of auger bit to emplace sensors and delay eventual melt out (images above).

Recovery Details: Sensors eventual melt out; no other details reported.

Sensors: Not reported.

Deployment Site: Greenland Ice Sheet.

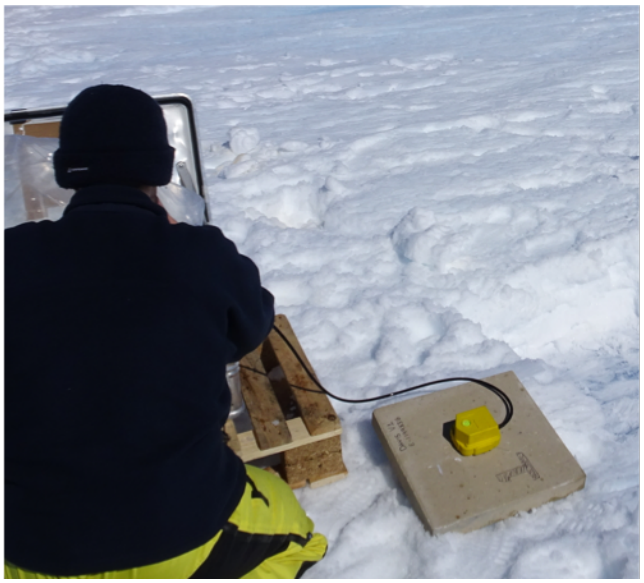

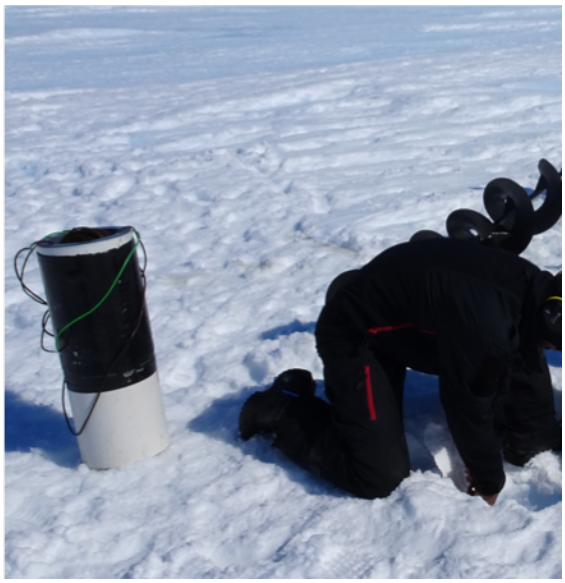

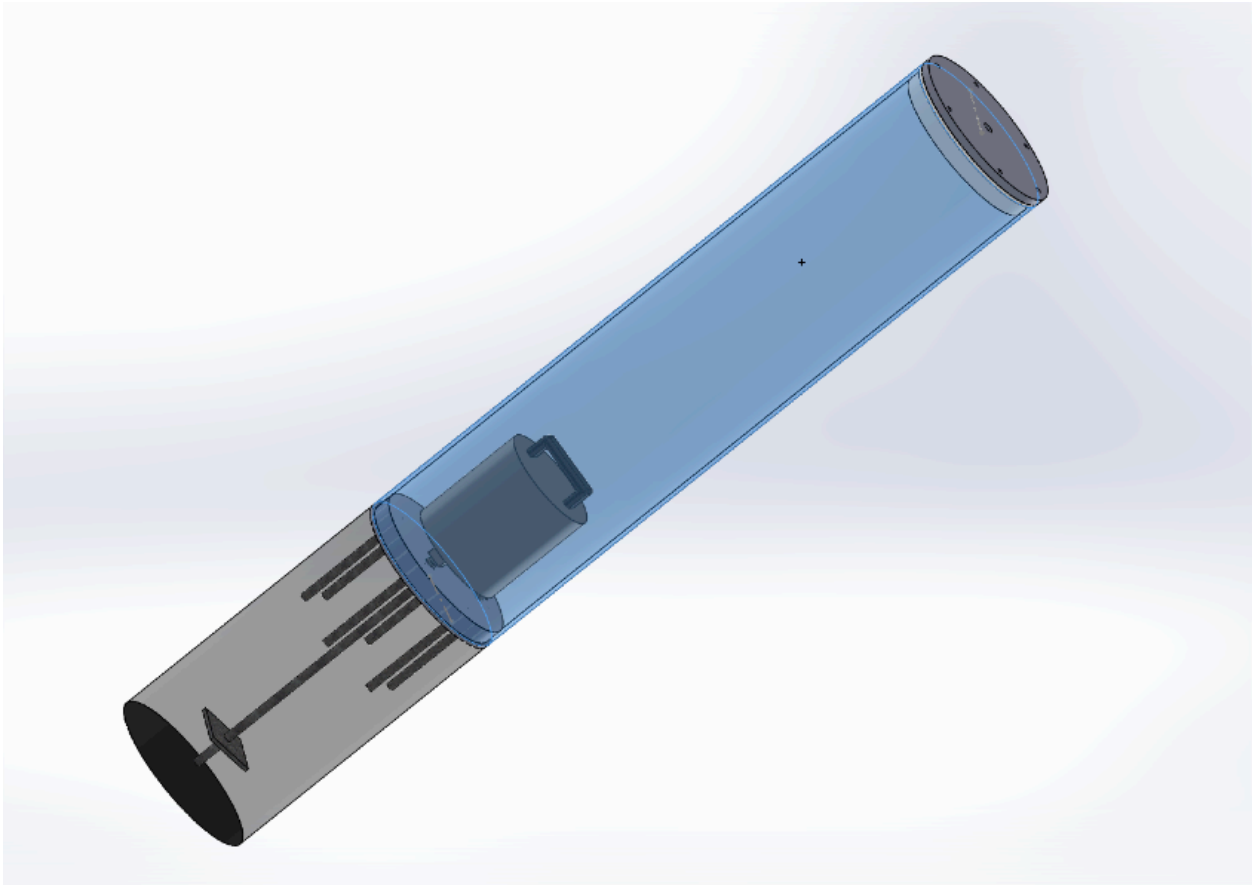

Investigators/Respondents: Sue Cook, Bernd Kulessa, and Glenn Jones.

Installation Method: Bolt geophone sensors to concrete paving slabs (images above); weight of slabs intended to keep geophone well coupled to ice during melt production (left). Place broadband seismometers in plastic casing vault with a concrete footing. The housing was deployed in the field using an ice auger with diameter only slightly larger than the seismometer housing (right).

Recovery Details: Sensors remain in field as of writing; Dr. Cook concerned about possible resonance imprint on time series.

Sensors: Broadband sensors and geophones.

Deployment Site: Antarctica Ice Sheet (Sørsdal Glacier).

GEOPHONE NLBS DATA SPECTROGRAMS

Figure S1 presents two additional spectrograms that we computed from the North (ELN) and vertical channels (ELZ) of geophone NLBS, over DOY 170 to DOY 250, 2011. We calculated these spectrograms, and the NLBS.ELE spectrogram displayed in Figure 2 of the main article, as follows: we process each data stream with a short-time Fourier Transform by first zero padding our data window from 150 s to 300 s. We then compute the spectrogram with 50% segment overlap, and taper our data with a Hamming window. After computation, we decimate the frequency axis by a factor of 10, and then decimate the time axis by a factor of four. Finally, we concatenated our spectrograms from each day into a single spectrogram and imputed missing data values with nearest neighbor interpolation.

LOW FREQUENCY SEISMIC EVENTS

Figure S2 shows multi-geophone, vertical channel observations of low frequency waveforms that arrived at nearly coincident arrival times at each receiver. The tectonic or glaciogenic sources of these waveforms are non-local (far outside the North Lake network). We found these waveforms by manually picking perceived icequakes from a visual review of vertical-channel spectrograms that we computed for each geophone. This search revealed population of 190 low frequency ($\leq$ 4.5 Hz peak frequency) events that consisted of waveforms with roughly 30 s duration signals (Figure S2) that were observable across the network. These events occurred daily, and exhibited no clear hourly bias in arrival time, from day to night. Because these events registered well below the 4.5 Hz peak frequency response of the L-28 geophone, their true waveform amplitudes are larger than that for higher-frequency events with the same-recorded amplitude.

CORRELATION DETECTORS

Correlation detectors (correlators) are digital waveform detectors that operate as pattern matching algorithms on seismic data (in this context). These detectors scan a template waveform that records a reference event against a noisy (target) data stream to compute a correlation statistic. The size of this correlation statistic relative to a threshold measures evidence that the target data contain a waveform matching the shape of the template waveform. The amplitude of any matching (target) waveform, relative to the target data noise variance, quantifies the performance of the correlation detector. Both the target waveform amplitude and data noise variance are unknown, and are only estimable from the data. Decision theory quantifies these concepts by deriving a correlation detector from a generalized likelihood ratio (GLR) under two competing hypotheses. The first (null) hypothesis $\mathcal{H}_0$ is that post-processed (detrended, tapered, and filtered) multichannel data $\boldsymbol{x}$ include only Gaussian noise $\boldsymbol{n}$ of unknown variance σ^2; computationally, $\boldsymbol{x}$ is a matrix whose columns store time series for each channel, in which row n indicates time sample n of each channel. The (alternative) hypothesis $\mathcal{H}_1$ assumes that post-processed data $\boldsymbol{x}$ include an amplitude-scaled copy of a template waveform $\boldsymbol{w}$ (amplitude A unknown) that is contaminated by Gaussian noise, also of unknown variance σ^2:

$$\begin{aligned} \mathcal{H}_0&: \ \boldsymbol{x} = \boldsymbol{n} \sim \mathcal{N}(\boldsymbol{0}, \sigma^2 \boldsymbol{I}) \\ \mathcal{H}_1&: \ \boldsymbol{x} = \boldsymbol{n} + A\boldsymbol{w} \sim \mathcal{N}(A\boldsymbol{w}, \sigma^2 \boldsymbol{I}) \end{aligned} \tag{S1}$$

Template $\boldsymbol{w}$ is a matrix that matches the size of $\boldsymbol{x}$ and $\boldsymbol{n}$; in practice, $\boldsymbol{w}$ includes very few non-zero samples that record the reference event, and the remaining rows are zero-padded. The GLR between the Gaussian probability density functions (PDFs) that describe these two competing hypotheses on the data $\boldsymbol{x}$ defines the correlation statistic $r(\boldsymbol{x})$, $(k = 0,1)$:

$$r(\boldsymbol{x};\mathcal{H}_k) = \frac{\mathrm{tr}(\boldsymbol{x}^{\mathrm{T}}\boldsymbol{w})}{\sqrt{\mathrm{tr}(\boldsymbol{x}^{\mathrm{T}}\boldsymbol{x})\mathrm{tr}(\boldsymbol{w}^{\mathrm{T}}\boldsymbol{w})}} \tag{S2}$$

in which tr(■) is the matrix trace operator, and the superscript T means transpose. This statistic is an estimate for the true, population correlation ρ_0 between the target data and template. Our correlator algorithm (Carmichael and Hartse, 2016; Carmichael, 2016) computes this ratio in the frequency domain, per 3600 s (one hour) processing window. The decision rule that forms the correlator compares $r(\boldsymbol{x})$ to a threshold η for detection:

$$r(\boldsymbol{x}) \underset{\mathcal{H}_0}{\overset{\mathcal{H}_1}{\gtrless}} \eta \tag{S3}$$

This conditional inequality states that the correlator selects $\mathcal{H}_1$ (a target waveform is detected) if $r(\boldsymbol{x})$ exceeds η, and selects $\mathcal{H}_0$ (data include only noise), if η exceeds $r(\boldsymbol{x})$. We use the Neyman Pearson criteria to compute the threshold η that maintains a predicted false-alarm-on noise probability $\mathrm{Pr}_{FA}^{\mathrm{Pre}}$ in the current processing window. This computation requires inverting probability density function (PDF) $f_R(r;\mathcal{H}_0)$ for the correlation statistic under $\mathcal{H}_0$:

$$f_R(r;\mathcal{H}_k) = \frac{(N_E-2)}{\sqrt{2\pi}} \frac{\Gamma(N_E-1)}{\Gamma\left(N_E-\frac{1}{2}\right)} \frac{\left(1-\rho_0^2\right)^{\frac{N_E-1}{2}}}{(1-r\rho_0)^{N_E-\frac{3}{2}}} (1-r^2)^{\frac{N_E-4}{2}} \, {}_2F_1\left(\frac{1}{2},\frac{1}{2};\frac{2N_E-1}{2};\frac{r\rho_0+1}{2}\right), \tag{S4}$$

in which ${}_2F_1(\ldots)$ is the Gaussian hypergeometric function whose first three arguments are parameters, whose last argument is a variable, and $\rho_0 = 0$ when $k = 0$ (Weichecki-Vergara and others, 2001). A corresponding estimate $\widehat{N}_E$ for the effective degrees of freedom N_E in the correlation time series $r(\boldsymbol{x})$ that shapes $f_R(r;\mathcal{H}_k)$ is:

$$\widehat{N}_E = \frac{\left(1-\rho_0^2\right)^2}{\widehat{\sigma}_R^2} + 1 \tag{S5}$$

in which $\widehat{\sigma}_R^2$ is the sample variance of $r(\boldsymbol{x})$ under $\mathcal{H}_k$. An estimator for $\widehat{\sigma}_R^2$ processes a semi-empirical target data stream with the original template, and then computes the variance of the resultant time series. This target data stream includes a wave-train composed of concatenated, independent noise vectors, or waveform template vectors ($[\boldsymbol{w}, \boldsymbol{w}, \ldots, \boldsymbol{w}]^{\mathrm{T}}$) added to commensurate, independent, noisy target data. With the PDF $f_R(r; \mathcal{H}_0)$ fully parameterized, we invert for the detector threshold η from:

$$\mathrm{Pr}_{FA}^{\mathrm{Pre}} = \int_{\eta}^{1} f_R(r; \mathcal{H}_0) dr \tag{S6}$$

that we set to $\mathrm{Pr}_{FA}^{\mathrm{Pre}} = 10^{-10}$. The predicted probability $\mathrm{Pr}_{D}^{\mathrm{Pre}}$ of detecting a waveform at this threshold is:

$$\mathrm{Pr}_{D}^{\mathrm{Pre}} = \int_{\eta}^{1} f_R(r; \mathcal{H}_1) dr \tag{S7}$$

Equation S6 and Equation S7 quantify the predictive capability of the correlation detector. We test our detector with a semi-empirical scheme, in which we inject multi-channel waveforms into real recorded noise, and then process the results with our multichannel correlation detector (Figure 3a of the main article shows template $\boldsymbol{w}(t)$). During this processing operation, we binned the empirical correlation statistics into normalized histograms and compare them to our theoretical PDF $f_R(r; \mathcal{H}_0)$ (Equation S4). The misfit between this (censored) histogram and the PDF curve quantifies our confidence in the data model described by Equation S1:

$$\epsilon_j = \left\| \mathrm{Hist}_{0.01}^{0.99}(r) - f_R(r; \mathcal{H}_0)|_{\widehat{N}_E} \right\|, \tag{S8}$$

in which j indexes the processing window, and data histogram $\mathrm{Hist}|_{Q2}^{Q1}(r)$ bins data within a particular quantile $Q1 < q < Q2$. We describe our process for selecting the three-channel

template waveform (Figure 3a) in the main article. With these representative waveforms chosen, we log-scaled each signal's amplitude to a prescribed value that we uniformly sampled from a 168-point grid. We assume that the template's icequake source has a particular, unknown seismic magnitude m_0 that relates to waveform amplitude. Our scaling then replaced each signal's original amplitude A_0 with a smaller amplitude A_l at grid point l:

$$A_l = 10^{m_l - m_0} A_0, \qquad m_l - m_0 \in [0, -1.75] \tag{S9}$$

where $m_l - m_0$ in Equation S8 is proportional to signature SNR (in decibels dB) and quantifies relative magnitude. Our scaling maintains the original, relative proportions of energy between all channels, but cannot accommodate any non-linear scaling in waveform shape that occurs with significant changes in magnitude. Regardless, we immersed each scaled waveform in thousands of noise observations that we recorded over pre- and resonance-coincident days (DOY 198-200 and DOY 218-220) and then processed our data with the correlator. To account for non-stationary noise, we estimated shaping parameters (e.g., degrees of freedom) for each statistics' PDF, in each detection window (hourly). We counted waveform detections N_{Dl} at each Δm_l grid point, and normalized N_{Dl} by the true number N_T of infused waveforms to construct observed detection curves against relative magnitude:

$$\left(m_l - m_0, \Pr_{Dl}^{\text{Obs}}\right) = \left(m_l - m_0, \frac{N_{Dl}}{N_T}\right), \tag{S10}$$

in which each curve is associated with a particular error ϵ_j (Equation S8); N_{Dl} and N_T are not to be confused with effective degrees of freedom $\widehat{N}_E$. Last, we time-averaged our empirical detection curves over all time windows to present the expected performance of the detector, and weighted curve "j" by ϵ_j^{-2} (Equation S8). Figure 3c of the main article shows these observed performance curves.

To quantify mis-match between the pre-resonance and resonance-coincident curves, we measure the range in magnitude Δm over which two different (weighted, time averaged) performance curves report the same probability of detection Pr_D:

$$\mathrm{Pr}_D^{(1)} = C, \text{ for } m - m_0 = m_1, \text{ and} \tag{S11}$$

$$\mathrm{Pr}_D^{(2)} = C, \text{ for } m - m_0 = m_2, \text{ then:}$$

$$\Delta m = m_2 - m_1$$

in which $C = 0.9$ in the main article. To interpret Equation S11, we note that if $\mathrm{Pr}_D^{(1)} = \mathrm{Pr}_D^{\mathrm{Obs}}(198 < \mathrm{DOY} < 200)$ and $\mathrm{Pr}_D^{(2)} = \mathrm{Pr}_D^{\mathrm{Obs}}(218 < \mathrm{DOY} < 220$ (for example), $m_2 = \Delta m + m_1$ measures the new magnitude at which the correlation detector can identify an icequake with probability $\mathrm{Pr}_D = 0.9$ (for example), when r is a test statistic. The conditions Equation S11 lists to estimate Δm are equivalent to graphical operations on performance curve plots. To execute these graphical operations, we find a horizontal line within a detection band that intersects curves $\mathrm{Pr}_D^{(1)}$ and $\mathrm{Pr}_D^{(2)}$. The horizontal range Δm between the intersection points of the resultant graph is the magnitude discrepancy.

REFERENCES

Carmichael JD, Hartse HE (2016) Threshold Magnitudes for a Multichannel Correlation Detector in Background Seismicity. *Bulletin of the Seismological Society of America*, **106(**2), 478-498 (doi:10.1785/0120150191)

Carmichael JD (2016) A Waveform Detector that Targets Template-Decorrelated Signals and Achieves its Predicted Performance, Part I: Demonstration with IMS Data. *Bulletin of the Seismological Society of America*, **106**(5), 1998-2012 (doi:10.1785/0120160047)

Wiechecki-Vergara S, Gray HL, and Woodward WA (2001) *Statistical Development in Support of CTBT Monitoring*. Southern Methodist University

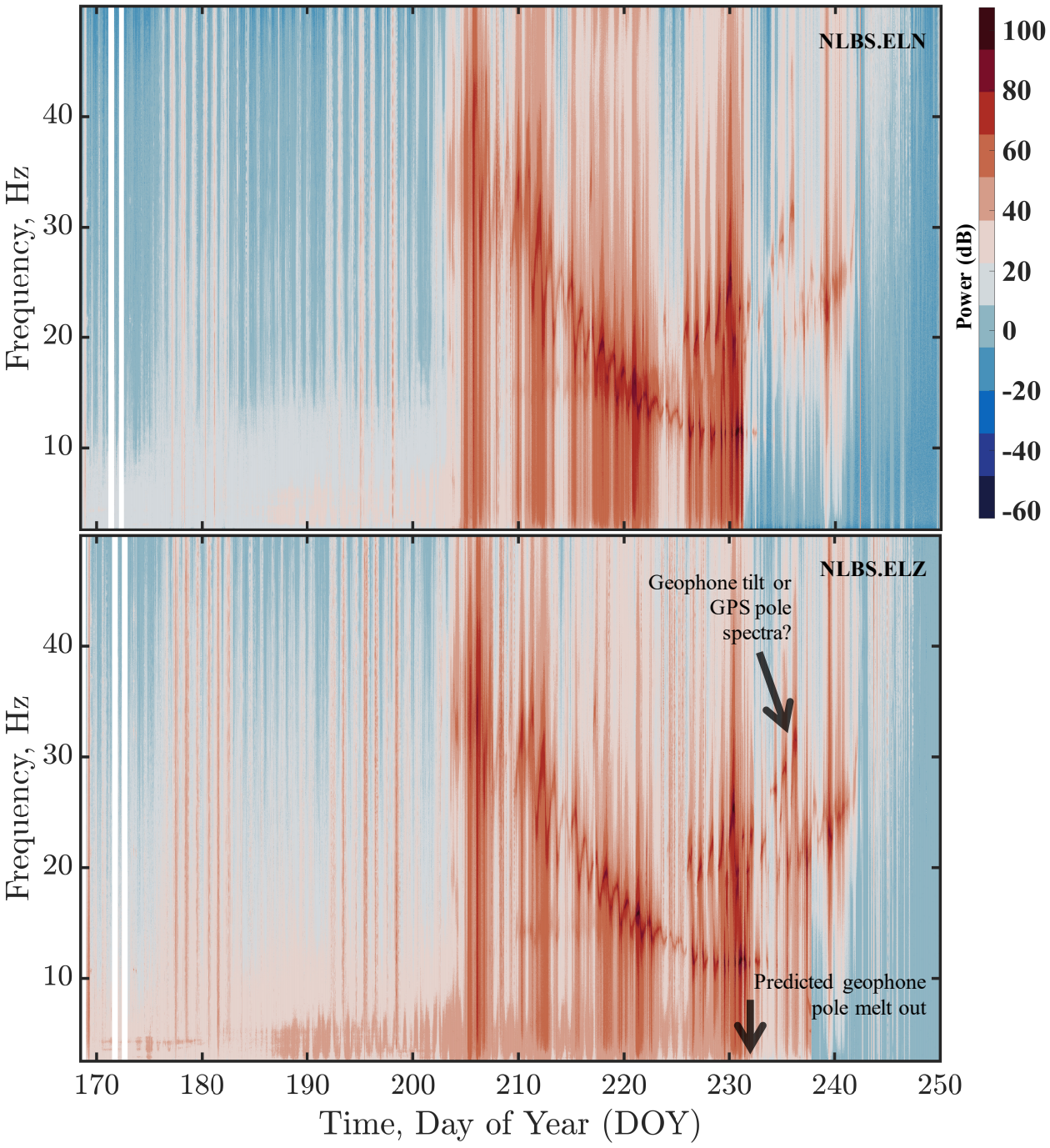

Fig. S1. North (ELN) and vertical channel (ELZ) spectrogram figures that we computed from the NLBS geophone over the same time duration (DOY 170-250, 2011) as shown for channel ELE in the main article (Figure 2, top).

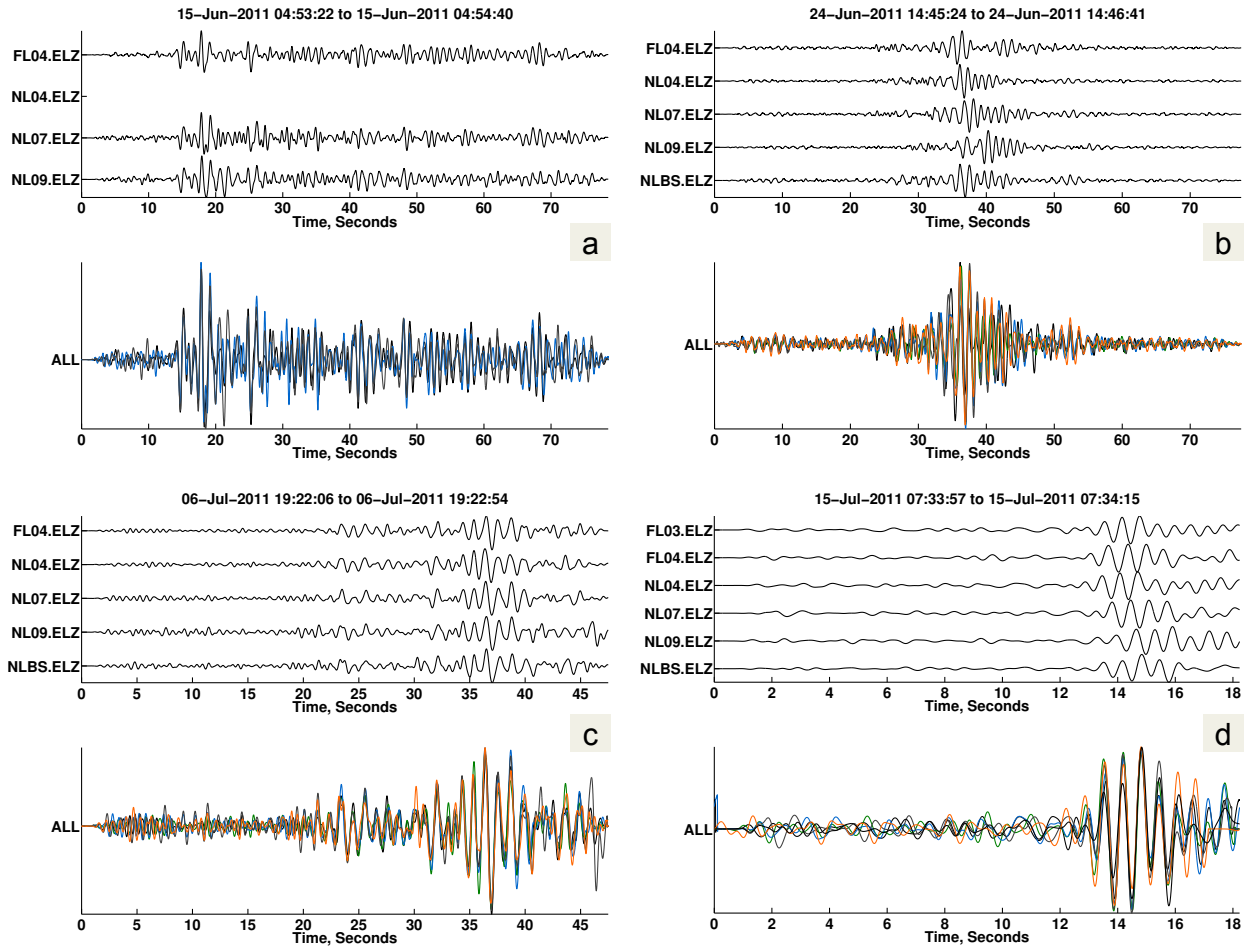

Fig. S2. Low frequency, vertical-channel velocity seismograms from the North Lake network (top, each panel) illustrated with a superposition of the same waveforms (bottom, each panel) that are labeled ALL and temporally aligned to maximize the intra-receiver waveform cross-correlation. Panels (a) through (d) show local to regional earthquakes observed days 166, 179, 187, and 196 that precede resonance. Our data do not show analogous events after resonance. The post-resonance absence of such waveforms suggests that melt out rendered geophones ineffective for recording signals even far outside the eigenfrequency band. The NL04 waveform data shown in (a) are available from IRIS, but are punctuated with ostensible timing problems and are therefore muted here.